Research Square

Preprints are preliminary reports that have not undergone peer review.
They should not be considered conclusive, used to inform clinical practice,
or referenced by the media as validated information.

# Cation effects on the electro-oxidation of alcohols are not mediated solely by their interactions with adsorbed OH

**Angel Cuesta**

acuesta@iqf.csic.es

CSIC

**Alan Gibson**

University of Aberdeen

**Tadeu Cabral**

Universidade Estadual de Campinas (UNICAMP)

**Victor Yukuhiro**

Universidade Estadual de Campinas (UNICAMP)

**Claudio Tormena**

Universidade Estadual de Campinas (UNICAMP)

**Pablo Fernández**

State University of Campinas https://orcid.org/0000-0002-5068-0556

**Article**

**Keywords:**

**Posted Date:** April 15th, 2026

**DOI:** https://doi.org/10.21203/rs.3.rs-9092202/v1

**License:** This work is licensed under a Creative Commons Attribution 4.0 International License.
Read Full License

**Additional Declarations:** There is **NO** Competing Interest.

# Cation effects on the electro-oxidation of alcohols are not mediated solely by their interactions with adsorbed OH

Alan J. Gibson[1], Tadeu Luiz Gomes Cabral[2], Victor Y. Yukuhiro[2,3], Claudio F. Tormena[2], Pablo S. Fernández[2,3] and Angel Cuesta[1,4,*]

[1]Advanced Centre for Energy and Sustainability (ACES), School of Natural and Computing Sciences, University of Aberdeen, Aberdeen, AB24 3UE, Scotland, UK

[2]Chemistry Institute, Universidade Estadual de Campinas (UNICAMP), 13083-970 Campinas, São Paulo, Brazil

[3]Center for Innovation on New Energies (CINE), Universidade Estadual de Campinas, 13083-841, São Paulo, Brazil

[4]Instituto de Química Física Blas Cabrera, CSIC, C. Serrano 119, E-28006 Madrid, Spain

*Corresponding Author: acuesta@iqf.csic.es; angel.cuestaciscar@abdn.ac.uk

## Abstract

In this work, we deconvolute the impact of electrolyte cations on the electro-oxidation of glycerol on Pt. UV-Vis reflectograms reveal that the presence of glycerol inverts and enhances the magnitude of cation effects on Pt oxidation. A cation-dependent glycerol diffusion coefficient was then identified using $^{1}$H-DOSY-NMR, providing solid experimental evidence that smaller cations interact more strongly with glycerol than larger ones. The rates of partial oxidation of glycerol to adsorbed carbon monoxide ($CO_{ad}$), and of $CO_{ad}$ oxidation, measured as a function of cation identity using time-resolved ATR-SEIRAS, suggest that global cation-induced trends in GOR activity are driven mainly by the reaction pathways that do not involve $CO_{ad}$. This implies that interactions between electrolyte cations and AOS alone cannot explain the cation-induced trends in electrocatalytic behaviour. Instead, the interactions of electrolyte cations with the reactant are critical to the cation-dependent electrocatalytic activity of alcohol and polyol oxidation.

The electro-oxidation of alcohols and polyols attracts considerable interest, driven by the need to transition away from fossil fuel-based sources of energy and raw materials. Alcohols and polyols can be easily stored and transported and can be sourced from waste streams or $CO_2$ conversion, making them attractive in applications from energy conversion and storage to the chemicals industry. Maximising energy efficiency is essential for such applications to be viable at scale. This requires a deep understanding of the reaction mechanism and dynamics over a wide range of conditions, to guide the intelligent design and implementation of next-generation catalyst materials and electrochemical reactors.

Particularly interesting is the glycerol oxidation reaction (GOR), for which Pt serves as a highly active model electrocatalyst. As a $C_3$ triol, glycerol oxidation is inherently complex, proceeding through a multiple-pathway mechanism.[1,2,3] One group of pathways, often termed indirect, involves breaking at least one of two C-C bonds and the dehydrogenation of the resulting C1 fragment(s) to yield adsorbed carbon monoxide ($CO_{ad}$), which can subsequently be oxidised to $CO_2$ ($CO_3^{2-}$ in alkaline medium). The second group, often termed direct pathways, encompasses any reaction pathway not involving $CO_{ad}$. The large overpotentials associated to $CO_{ad}$ oxidation is a significant factor limiting the energy efficiency of alcohol or polyol oxidation.

Electrolyte cations can have a pronounced influence on electrocatalytic reactions,[4-8] including the electro-oxidation of alcohols and polyols.[9-14] Using surface-enhanced infrared absorption spectroscopy in the attenuated total reflection mode (ATR-SEIRAS), Yukuhiro *et al*.[13] recently

offered a new interpretation of the effect of alkali-metal cations in alkaline electrolytes on the activity of Pt for the oxidation of several alcohols and polyols, superseding the blocking effect proposed ca. 17 years ago by Strmcnik *et al*.[15] They demonstrated that, in 0.1 M glycerol, both the potential at which $CO_{ad}$ disappears from the surface and that at which the surface is de-activated through the formation of an inactive Pt oxide shift positively following the trend $Li^+ < Na^+ < K^+$. This implies that cations either alter the relative rates of formation and oxidation of $CO_{ad}$, or perturb the competition for adsorbed oxygenated species (AOS) between surface oxidation and the several parallel pathways involved in alcohol and polyol oxidation.

In this work, we explore these two possibilities. We show that the cation-induced shift in the onset of Pt oxidation is reversed in 0.1 M glycerol as compared to its absence. Based on that, we show that cation effects cannot be due solely to the interaction of the cation with the surface or with AOS. Instead, their interaction with the reactant itself and with reaction intermediates must also be considered.

## Results

Cation effects on Pt oxidation. CVs of a polycrystalline Pt disc ($Pt_{poly}$) in 0.5 M MOH (M = $Li^+$ (black), $Na^+$ (red), $K^+$ (blue)) and in 0.5 M MOH + 0.1 M glycerol are presented in Figs. 1A and B, respectively. Similar CVs can be found elsewhere.[1-3,12-14] In the positive-going scan of Fig. 1B, the surface is blocked between ca. 0.07 and 0.45 V by $CO_{ad}$ formed through partial glycerol oxidation.[13] This is possible due to the presence of adsorbed OH ($OH_{ad}$) on low-coordinated surface sites at potentials at least as low as 0.1 V.[16,17] Glycerol oxidation re-initiates at $E > 0.45$ V, coinciding with the beginning of $CO_{ad}$ oxidation,[13] leading to the main oxidation peak. The peak potential falls between 0.78 V and 0.88 V. After the peak, a significant reduction in glycerol oxidation current is observed. Both peak potential and peak current follow the trend $Li^+ < Na^+ < K^+$.

Recently,[13] we have shown that this activity trend, common to several, if not all, alcohols and polyols, arises from the formation of an inactive Pt oxide layer on the surface. In-situ X-ray Absorption Spectroscopy (XAS) showed that the potential at which this occurs follows the trend $Li^+ < Na^+ < K^+$.[13] However, the effect of the cation on the formation of Pt oxide *in the absence of glycerol* was not probed in that work. We employ now UV–vis reflectance to probe Pt oxide formation both in the presence and absence of glycerol. UV-vis reflectance is more sensitive than XAS to metal surface oxidation because, due to metals' very short Thomas-Fermi length, potential-induced changes in reflectance arise exclusively from the top surface layer. It requires in addition a much simpler and cheaper experimental set-up and, unlike XAS, does not require access to synchrotron radiation or the use of very small nanoparticles to minimize contributions from the bulk.

Figs. 1C, D and E show reflectograms at $\lambda = 500$ nm in 0.5 M LiOH, NaOH, and KOH, respectively, in the absence (thin lines) and presence (bold lines) of 0.1 M glycerol. When glycerol is present, negative of the main glycerol oxidation peak, the reflectance shows a small linear, cation-independent increase with increasing potential, due mainly to the electroreflectance of $CO_{ad}$-covered Pt.[18] Conversely, in the absence of glycerol, the reflectance at 500 nm in this region displays a small, linear decrease, due either to the electroreflectance of Pt or to a continuous increase in the coverage of AOS. In the absence of glycerol, the reflectance in the positive-going scan starts decreasing faster at ca. 0.73 V, due to Pt oxidation (Figs. 1C-E, vertical dashed pink line), which extends to the positive limit of the CV at 1.3 V. Between 1.3 V and 0.5 V in the negative scan, the reflectance increases again and returns to its value before oxidation following reduction of the oxide. Both the CVs (Figs. 1A and S4A) and the reflectograms at $\lambda = 500$ nm (Figs. 1C-E and S4B) and $\lambda = 250$ nm (Fig. S4C) in the absence of glycerol suggest that the onset of Pt oxidation in the positive-going scan occurs at a potential that follows the trend $Li^+ > Na^+ > K^+$. Although the differences in the glycerol-free reflectograms are just above experimental error, they are reproduced at 500 and 250 nm (Figs. S4B and C). Furthermore, this result is in agreement with previous work,[19,20] in which both the positive shift in the H-adsorption/OH-desorption peaks and the negative shift of the onset of Pt oxidation when

going down the alkali-metal group were attributed to a destabilisation of adsorbed $OH_{ad}$ by the cation that follows the trend $Li^+ < Na^+ < K^+$.

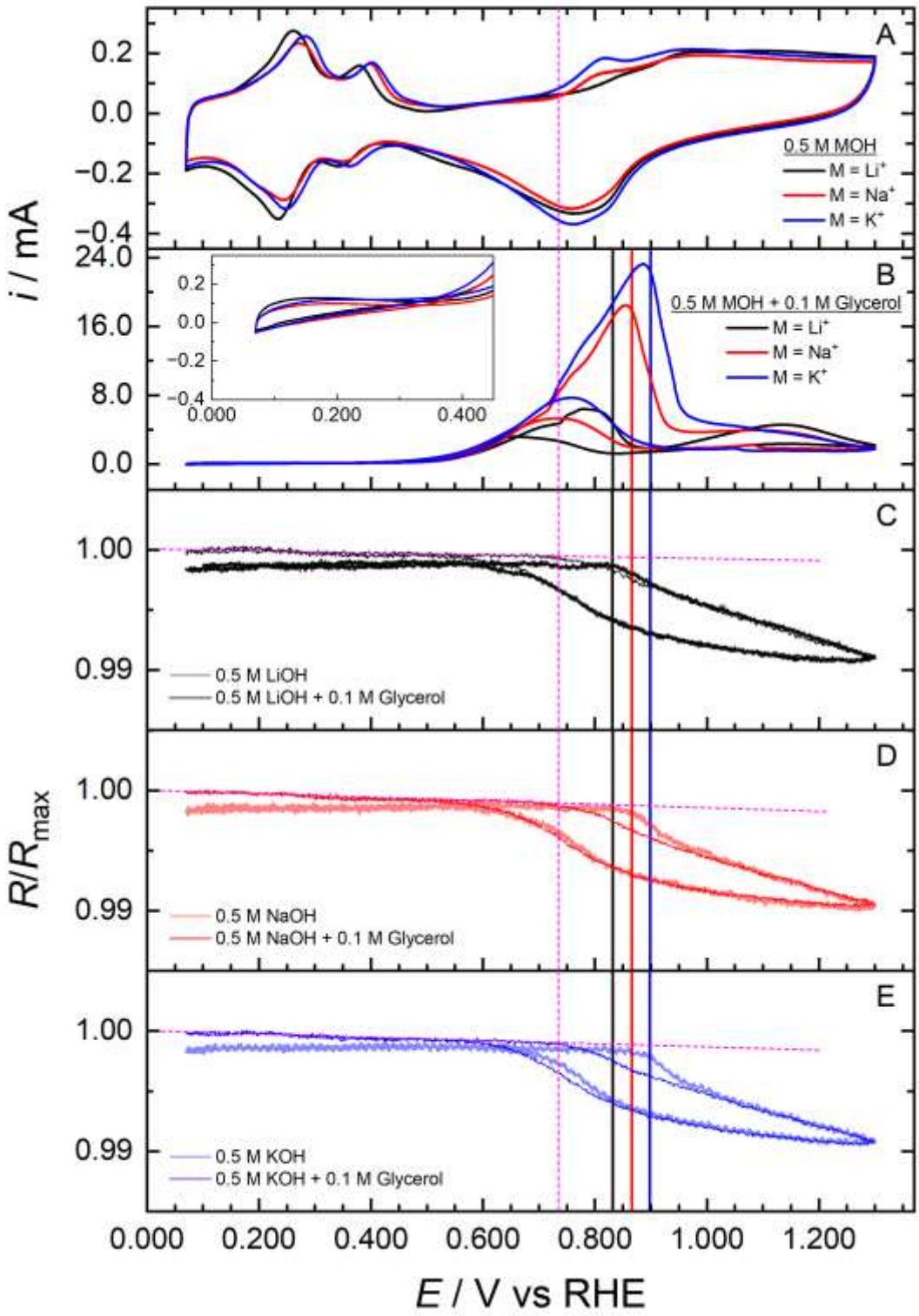



**Figure 1.** CVs of $Pt_{poly}$ in 0.5 M MOH (M = $Li^+$ (black), $Na^+$ (red), $K^+$ (blue)) without **(A)** and with **(B)** 0.1 M glycerol, scan rate = 50 mV $s^{-1}$. **(C-E)** Reflectograms recorded synchronously with these CVs at $\lambda$ = 500 nm in 0.5 M MOH, both without (thin line) and with (bold line) 0.1 M glycerol, in 0.1 M LiOH **(C)**, NaOH **(D)** and KOH (**E**). Intersecting pink dashed lines indicate the beginning of Pt oxidation in the absence of glycerol, whilst solid vertical black, red and blue lines indicate the beginning of the same process in the presence of glycerol in LiOH, NaOH and KOH, respectively.

The cation effect on Pt oxidation *in the absence* of glycerol described above is exactly the opposite of that recently reported[13] and now confirmed by us (Fig. 1C-E, solid vertical lines) *in the presence* of glycerol. For each cation, comparing the reflectograms in the presence and absence of glycerol confirms the expected positive shift in the onset of Pt oxidation when an alcohol/polyol is present[13,21-23] (Fig. 1C-E, compare dashed and solid vertical lines), due to the competition between the GOR and Pt oxidation for AOS.[24] The magnitude of that shift clearly increases going down the alkali-metals group, leading to reversal of the trend in Pt oxide formation (in 0.1 M glycerol, $Li^+ < Na^+ < K^+$). Once initiated, surface oxidations proceeds briefly at an accelerated rate, until the reflectance profiles with and without glycerol coincide at a potential also following the trend $Li^+ < Na^+ < K^+$. We have recently shown[23] that this corresponds to the potential at which $CO_{ad}$ disappears from the electrode surface. The reflectograms therefore confirm that the potential at which $CO_{ad}$ disappears from the Pt surface in 0.1 M glycerol follows the trend $Li^+ < Na^+ < K^+$.[13]

The trend reversal in the onset of Pt oxidation in 0.1 M glycerol strongly suggests that the interaction between cations and AOS alone cannot account for the GOR reactivity trend. Otherwise, that trend would mimic that of Pt oxidation in the absence of glycerol. It is therefore necessary to probe glycerol-cation interactions experimentally and quantitatively, to assess the effect this could have on cation-induced GOR activity trends.

Interactions between cations and glycerol. A recent study[14] of the GOR on a Pt RDE in alkaline media reported that an increase in the rotation rate, and therefore in the rate of transport of glycerol to the electrode surface, increased GOR currents only in $Na^+$- or $K^+$-containing electrolytes, no effect being observed with $Li^+$. However, the increase with $Na^+$ and $K^+$ was small and did not follow the expected dependence on the rotation rate. (Please note, even at low glycerol concentrations, at best a mixed kinetic-transport control region can be observed on Pt electrodes.)

This prompted us to use $^1$H-DOSY-NMR to directly investigate glycerol–cation interactions and their possible influence on glycerol diffusion. Fig. 2A shows that the diffusion coefficient of glycerol in KOH ($D_K$) and LiOH ($D_{Li}$) decreases linearly with increasing concentration (see Supporting Information, Section S5, Tables S1-S14 and Figs. S5-S17, for further details). Because the viscosities of both solutions are similar,[25] Fig. 2A implies an increasing concentration of glycerol molecules directly interacting with the corresponding cation with increasing ionic strength. Furthermore, because the slope is larger with $Li^+$ than with $K^+$, $Li^+$ must interact more strongly with glycerol than

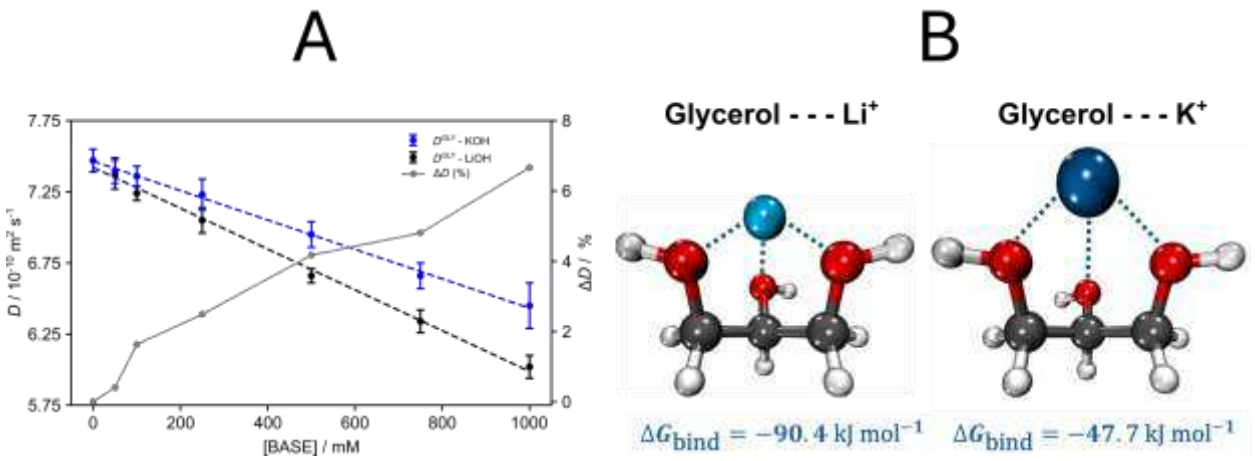



**Figure 2. (A)** Variation of the diffusion coefficient of glycerol ($D$, in $10^{-10}$ m$^2$ s$^{-1}$) and the relative difference between the glycerol diffusion coefficients in the presence of $K^+$ and $Li^+$ ($\Delta D$, in %) as a function of KOH and LiOH concentrations in deuterated water, measured by $^1$H-DOSY-NMR (400 MHz) at 298.15 K. **(B)** Optimized DFT lowest-energy structures and corresponding Gibbs free energies of binding ($\Delta G_{bind}$) computed at the ωB97X-D4/def2-TZVPD/SMD(water) for glycerol interacting with $Li^+$ (left) and $K^+$ (right).

$K^+$. However, $D_K$ and $D_{Li}$ differ by only ~4% at 0.5 M MOH. Even if the GOR were purely diffusion-controlled, such a small difference in $D$ would translate into at most a ~2.5% difference in the measured currents (diffusion-limited currents scale as $D^{2/3}$), much smaller than the cation-induced differences in activity (Fig. 1B). The effect of rotation should also be stronger with $Li^+$ than with $K^+$. Instead, $Li^+$ was the only case in which electrode rotation did not perturb the GOR current.[14]

Density functional theory (DFT) calculations were performed to evaluate the thermodynamics of solvation of $K^+$ and $Li^+$ by glycerol (see SI, Section S6, Table S15). The resulting optimized structures for glycerol-cation complexes are shown in Fig. 2B. Unsurprisingly, they suggest the interaction occurs between the cation and the OH group of the alcohol. The computed Gibbs free energy ($\Delta G_{bind}$) of the interaction of glycerol with $K^+$ is –47.7 kJ·mol$^{-1}$, which increases to –90.4 kJ·mol$^{-1}$ with $Li^+$. I.e., the interaction between glycerol and $Li^+$ is 42.7 kJ·mol$^{-1}$ stronger than with $K^+$.

Combined, these observations indicate that there indeed exists an interaction between alkali-metal cations and glycerol, but the effect of such interaction on glycerol diffusion cannot account for the cation-dependent behaviour observed in Fig. 1 and elsewhere. Once an effect on transport of the reactant to the surface has been discarded, any effect of this cation-glycerol interaction must emerge from it affecting the rates of one or several GOR reaction pathways. Our previous work[13] and the results presented here show beyond any doubt that cation effects on GOR activity are related with the effect of the cation on the potentials at which $CO_{ad}$ disappears from the surface and at which Pt is oxidised. We decided, therefore, to test next how cations affect the rates of $CO_{ad}$ formation and $CO_{ad}$ oxidation.

Time-resolved ATR-SEIRAS: $CO_{ad}$ formation and oxidation. Time-resolved spectral series in 0.5 M MOH + 0.1 mM glycerol (M = $Li^+$ and $K^+$) after a potential step from 0.6 V to 0.25 V (at 0.25 V, $CO_{ad}$ formation is the dominant, if not the only, reaction) are presented in the SI (section S7, Figs. S18 and S19; the corresponding current transients are shown in Fig. S20). A glycerol concentration of 0.1 mM was used, as $CO_{ad}$ forms too fast at higher concentrations for the highest time resolution we can achieve. As shown below, using dilute glycerol solutions has the added benefit that $CO_{ad}$ disappears from the surface before the onset of Pt oxidation.

Figs. 3A and 3B show the time evolution of the integrated intensities of the bands corresponding to $CO_L$, $CO_B$ + $CO_M$ and their sum (Total $CO_{ad}$). The time-derivatives of these integrated intensities are shown in Figs. 3C and 3D. The value of the time-derivatives of these integrated intensities at $t$ = 0 must correspond to the rate of formation of the corresponding species on the $CO_{ad}$-free Pt surface. Inspection of the traces in Fig. 3 reveals that $dI_{CO}/dt$ for Total $CO_{ad}$ (i.e., the rate of $CO_{ad}$ formation from glycerol) at $t$ = 0 is the same for $Li^+$ and $K^+$.

The formation of $CO_B$ + $CO_M$ though is clearly favoured initially over that of $CO_L$, and much more so with $K^+$ than with $Li^+$. This has been observed before and is attributed to cation-dependent changes in the interfacial electric field.[26] In fact, Total $CO_{ad}$ at $t$ = 0 for $K^+$ in Fig. 3D consists only of $CO_B$ + $CO_M$. Once $CO_L$ starts to form on the surface with $K^+$, $\theta_{CO}$ increases faster with $K^+$ than with $Li^+$ and the rates of $\theta_{CO}$ increase with $K^+$ and $Li^+$ diverge. This prompted us to examine in more detail how the rates at which $\theta_{CO}$ increases and decreases depend on potential in 0.1 mM glycerol, by recording ATR-SEIRA spectral series during CVs at 5 mV s$^{-1}$.

Fig. 4A shows the forward scan of the first voltametric cycles, and Figs. 4B and C show the integrated intensities of $CO_L$, $CO_B$ + $CO_M$ and Total $CO_{ad}$ as well as their derivatives, as a function of potential. The first and second CVs at 50 and 5 mV s$^{-1}$, the complete spectral series, spectra between 2200 and 1150 cm$^{-1}$ extracted from the spectral series at 100 mV intervals in the positive-going scan of the first cycle, and a description of all the bands observed in the spectra are provided for reference in the SI (Section S7, Figs. S21-S24).

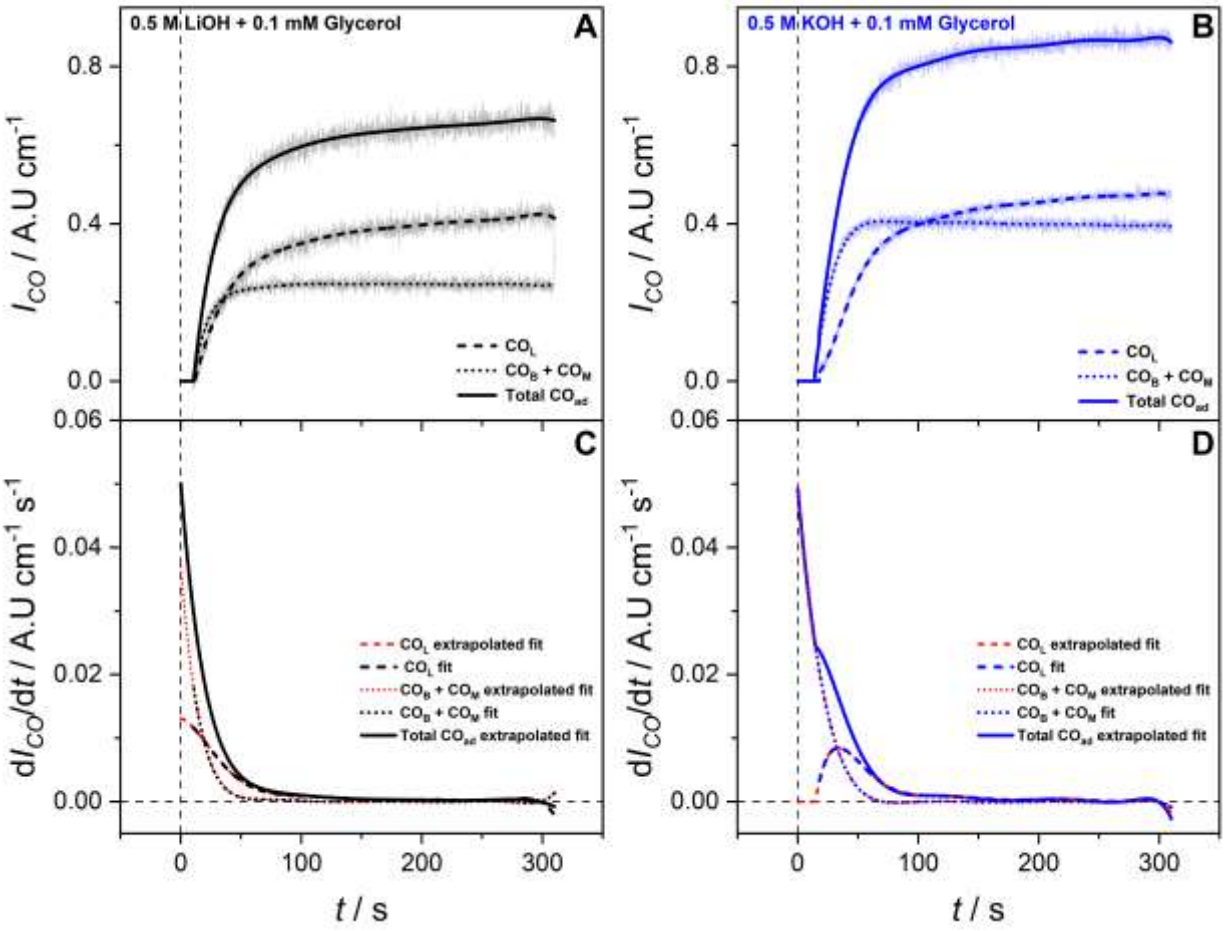



**Figure 3.** Upper panels **(A** and **B):** Integrated intensities of the IR bands corresponding to $CO_L$ (dashed line), $CO_B$ + $CO_M$ (dotted line) and the sum of the two (solid line) adsorbed on Pt, as a function of time after a potential step from 0.6 V-0.25 V in 0.5 M MOH + 0.1 mM $C_3H_8O_3$, with M = $Li^+$ **(**black lines, **A)** and $K^+$ **(**blue lines, **B)**. Bold lines in panels A and B are order 9 polynomial fits of the raw integrated intensity data, which is shown underlaying these fits in black shading, down to the spectrum immediately preceding the first observation of each band. Lower panels **(C** and **D)**: the time-derivative of the integrated intensities plotted in the upper panel, as a function of time for $Li^+$ **(C)** and $K^+$ **(D)**, with the same colour and line-type scheme. Red dashed lines show the extrapolation of the derivatives to $t = 0$.

At this low glycerol concentration, the Pt surface remains $CO_{ad}$-free ($\theta_{CO}$ = 0) after stepping the potential from 0.6 V to 0.1 V prior to recording the CV. $CO_{ad}$ emerges at the same potential for both cations (Figs. 4B and C), coinciding with the onset of the peak centred at 0.25 V in the CV (Fig. 4A), which is consistent with Fig. 3. This peak therefore results from the oxidation of glycerol to $CO_{ad}$. In the second cycle this peak is almost absent in the CV (Fig. S21) and $CO_{ad}$ is observed down to 0.07 V (Fig. S22), as it has had time to accumulate at potentials positive of the peak at 0.25 V when approaching the negative limit of the CV in the first negative-going scan. Also consistent with Fig. 3, while $CO_L$ and $CO_B$ + $CO_M$ emerge at the same potential with $Li^+$, with $K^+$ $CO_B$ + $CO_M$ appears first and $CO_L$ is only detected some tens of millivolts later. However, the maximum rate of increase of $\theta_{CO}$, which occurs slightly after the peak at 0.25 V (Fig. 4A), is larger for $K^+$ than for $Li^+$. This is again consistent with Figs. 3C and D, according to which once $CO_L$ appears on the surface in the $K^+$-containing electrolyte, $\theta_{CO}$ increases faster with $K^+$ than with $Li^+$. This leads to a higher maximum $\theta_{CO}$ with $K^+$ than with $Li^+$, reached at ca. 0.45 V in both cases, around the onset of the main oxidation peak (Fig. 4A). At this potential, $dI_{CO}/dE = 0$ in both cases, i.e., the rate of $CO_{ad}$ formation equals that of its oxidation with both cations.

The rest of the features observed in Figs. 4B and C are analogous to those reported by Yukuhiro *et al.*[13] in 0.1 M glycerol, except, importantly, for the potential at which $CO_{ad}$ disappears from the surface. As oxidation of $CO_{ad}$ becomes faster than its formation and $I_{CO}$ starts to decrease with both

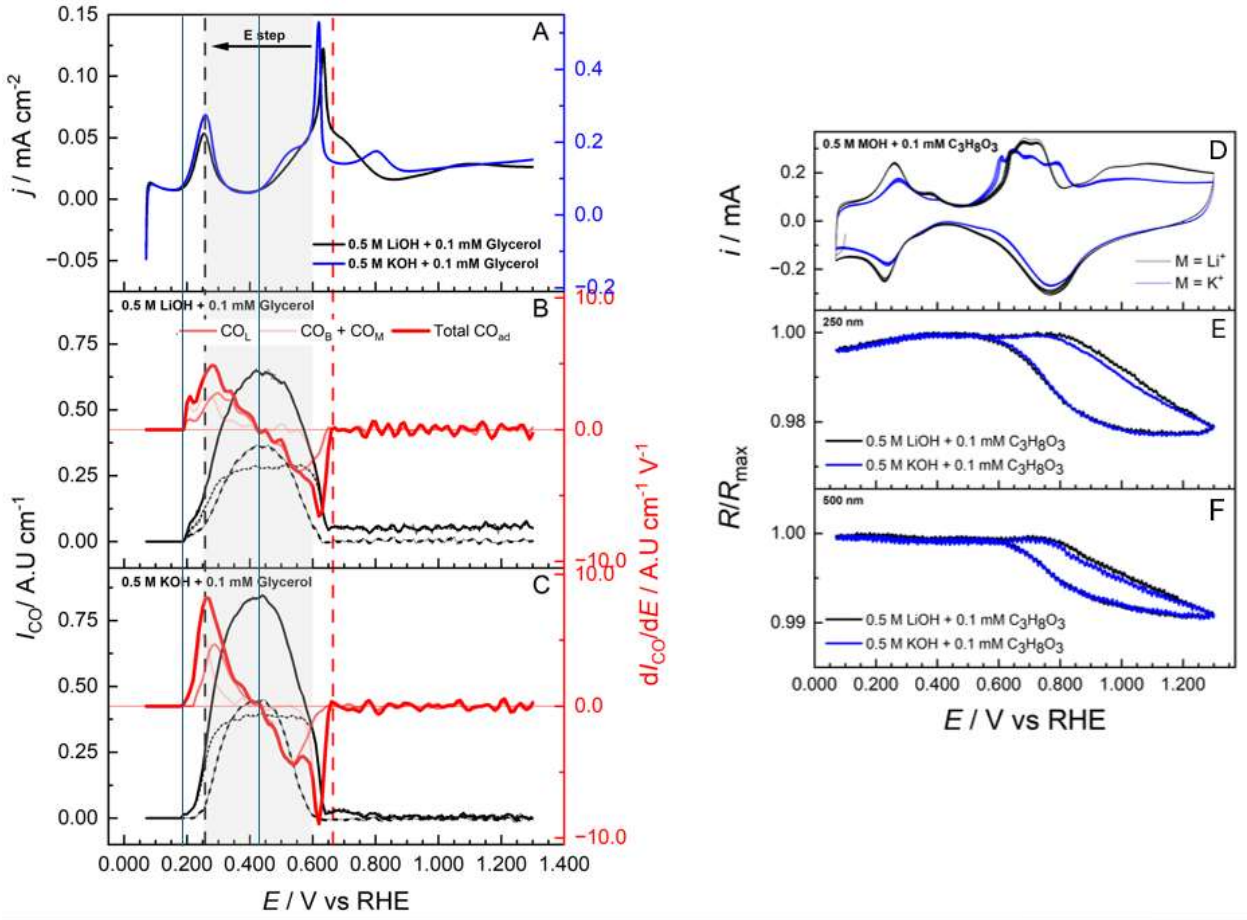



**Figure 4. Left: (A)** Positive going scan of the first cycle of a CV of $Pt_{poly}$ in 0.5 M MOH + 0.1 mM $C_3H_8O_3$, with M = $Li^+$ (black line) and $K^+$ (blue line), recorded after stepping the potential from 0.6 V to 0.1 V, scan rate = 5 mV/s. The complete CVs can be found in Fig. S5B of the SI. Integrated intensities as a function of potential for $CO_L$ (dashed line) $CO_B$ + $CO_M$ (dotted line) and total $CO_{ad}$ (i.e., the sum of the two, solid line) are also presented, recorded synchronously with the CVs in (A) in LiOH **(B)** and KOH **(C)** containing electrolytes. Shaded red lines in panels (B) and (C) correspond to the potential derivatives of these integrated intensities. Horizontal thin red lines mark $dI_{CO}/dE = 0$. The vertical dashed black line marks the peak maxima in the CVs, at ca. 0.25 V. The red vertical line marks the potential at which $CO_{ad}$ is removed from the surface. Solid black vertical lines mark the potential at which $CO_{ad}$ emerges and $dI_{CO}/dE = 0$ at $I_{CO}$ (max). The grey shaded region marks the limits of the potential step program used in the time-resolved IR experiments. Spectroscopic data was calculated from the series shown in Fig. S6B1 and S6B2. **(D)** CVs of a $Pt_{poly}$ disc electrode in contact with 0.5 M MOH + 0.1 mM glycerol (M = $Li^+$ (black), $K^+$ (blue)), scan rate = 50 mV/s, along with reflectograms recorded synchronously with these CVs at λ = 250 nm **(E)** and 500 nm **(F)**, obtained by co-adding 8-10 individual reflectance experiments.

cations after 0.45 V, we observe that the maximum rate of decrease of $\theta_{CO}$ is actually higher with $K^+$ than with $Li^+$ (Figs. 4B and C), the opposite to expectations based on previous studies of cation effects on $CO_{ad}$ stripping in alkaline media in the absence of a CO source.[9] This implies that when $CO_{ad}$ is simultaneously being generated and consumed during an electrocatalytic reaction, cation effects on the $CO_{ad}$ oxidation component of the reaction cannot be extrapolated from CO-stripping data.

It is then remarkable that, in 0.1 mM glycerol, $CO_{ad}$ disappears from the surface at the same potential for both cations (ca. 0.66 V, Figs. 4B and C), around 0.1 V before the onset of Pt oxidation. Furthermore, the effect of the cation on the onset of Pt oxidisation now reverts to that in the absence of glycerol (i.e., $K^+ < Li^+$), as shown by the reflectograms at 50 mV $s^{-1}$ in Fig. 4D-F. In other words, the competition between alcohol and Pt oxidations for AOS, which resulted in a reversal of the trend in the cation-dependent onset of Pt oxidation in 0.1 M glycerol, is absent in 0.1 mM glycerol.

## Discussion

The effect of alkali-metal cations on the activity of Pt for the oxidation of alcohols and polyols is associated with the effect those cations have on the onset of Pt oxidation. This effect is larger, and occurs in the opposite direction, in the presence compared to the absence of the alcohol or polyol. Such reversal can only be due to cations affecting the kinetics of AOS removal by the alcohol or polyol oxidation itself, as the rate of consumption of AOS by Pt oxidation must be essentially the same with and without the reactant. The insensitivity of the reflectograms to the presence of glycerol once $CO_{ad}$ has disappeared from the surface (Fig. 1) further confirms this. Electrolyte cations must therefore modify the competition between the alcohol or polyol oxidation and that of the Pt surface for AOS.

The rate of formation of $CO_{ad}$ from glycerol on the $CO_{ad}$-free Pt surface is cation independent at $\theta_{CO} = 0$ (Fig. 3), but becomes faster with $K^+$ than with $Li^+$ when $CO_L$ emerges in the $K^+$-containing electrolyte, after which $\theta_{CO}$ increases faster with $K^+$ than with $Li^+$. Would this balance persist, we would expect $CO_{ad}$ to survive on the surface up to a more positive potential with $K^+$ than with $Li^+$. Although this is indeed the case in 0.1 M glycerol, in 0.1 mM glycerol $CO_{ad}$ disappears from the Pt surface at the same potential (0.66 V, around 0.1 V negative of the onset of surface oxidation) with both $Li^+$ and $K^+$. Furthermore, in 0.1 mM glycerol, the potential at which $\theta_{CO}$ is maximum and $dI_{CO}/dE = 0$ is the same (ca. 0.45 V) with both cations. At this point, the rates of $CO_{ad}$ formation and oxidation must be identical: if formation is faster with $K^+$ than with $Li^+$, so must be oxidation. In fact, as we continue scanning positive towards the main oxidation peak, we observe that $\theta_{CO}$ decreases faster with $K^+$.

To summarise (Fig. 5), we can identify five potential regions:

i. An initial regime (around 0.1 V) where the rate of $CO_{ad}$ formation is the same with both cations and the rate of $CO_{ad}$ oxidation is zero.[9,27]

ii. A regime in which $CO_{ad}$ formation is faster with $K^+$ than with $Li^+$ and faster than $CO_{ad}$ oxidation in both cases, but the difference between the rate of $CO_{ad}$ formation and that of $CO_{ad}$ oxidation is larger with $K^+$ than with $Li^+$.

iii. A potential (ca. 0.45 V) at which the rates of $CO_{ad}$ formation and oxidation are equal to one another with both cations. If the rate of $CO_{ad}$ formation is faster with $K^+$ than with $Li^+$ as in regime (ii), then also the rate of $CO_{ad}$ oxidation will now be faster with $K^+$ than with $Li^+$.

iv. A regime in which $CO_{ad}$ oxidation is faster than $CO_{ad}$ formation with both cations and in which, as in (ii), the difference between them has to be larger with $K^+$ than with $Li^+$.

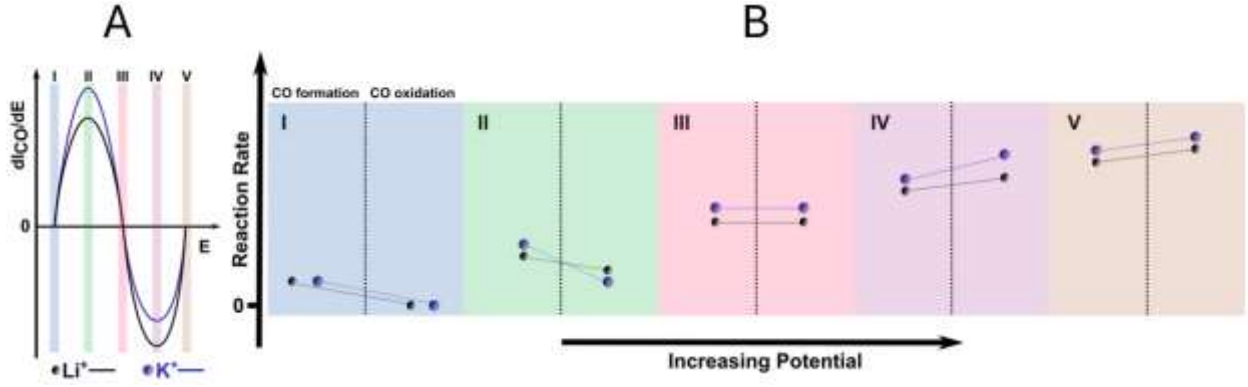



**Figure 5. (A)** Schematic representation of the $dI_{CO}/dE$ vs. $E$ traces obtained from in-situ voltametric ATR-SEIRAS series in 0.5 M LiOH (black lines) and KOH (blue lines) containing 0.1 mM glycerol reported in Figs. 4B and 4C. Coloured vertical stripes highlight critical points at which specific regimes of relative rates of $CO_{ad}$ formation and oxidation must exist, as described in the main text. **(B)** Diagram depicting qualitatively how the relative rates of $CO_{ad}$ formation and oxidation with $Li^+$ and $K^+$ must progress across regimes (i)-(v) in (A).

v. A final regime in the limit of low $\theta_{CO}$, in which the difference between the rates of $CO_{ad}$ formation and oxidation must be identical for $Li^+$ and $K^+$, because the potential at which $CO_{ad}$ disappears from the surface (0.66 V) does not depend on the cation (Fig. 4A-C).

The obvious question then is why, in 0.1 M glycerol, does $CO_{ad}$ survive up to, and why does catalyst surface deactivation occur at, more positive potentials moving from $Li^+$ to $K^+$. While in 0.1 mM glycerol $\theta_{CO}$ becomes zero before the onset of Pt oxidation (Fig. 4A-C), in 0.1 M glycerol $CO_{ad}$ survives well into the Pt oxide region (reference [13] and Fig. 1). At the same time, at low glycerol concentration the onset of Pt oxidation is unaffected by the presence of glycerol (compare Figs. 4D-F and S4). In other words, at low glycerol concentration, the combined rates of all the GOR pathways cannot outcompete Pt oxidation for AOS. We have also shown that cation-induced differences in the relative rates of $CO_{ad}$ formation and oxidation cannot explain cation effects on the potential at which $CO_{ad}$ is removed from the surface and Pt oxidises at higher glycerol concentrations. We conclude, therefore, that at high glycerol concentration (i) the potential at which $CO_{ad}$ is removed from the surface, (ii) the trend reversal in cation effects on the potential at which Pt oxidises, and (iii) the global cation-induced trends in GOR activity (in all cases, $Li^+ < Na^+ < K^+$), must be due to an effect of the cation on the rates of the GOR pathways that do not involve $CO_{ad}$. Because the rate of these pathways must scale with the glycerol concentration, in 0.1 mM glycerol removal of AOS by them is not fast enough to affect the onset of Pt oxidation, which proceeds as in the absence of glycerol. At high glycerol concentration, these pathways remove AOS, needed for both $CO_{ad}$ and Pt oxidation, faster, shifting the complete removal of $CO_{ad}$ and the onset of Pt oxide formation positively. Because the magnitude of this positive shift increases along the sequence $Li^+ < Na^+ < K^+$, we must conclude that so too do the rates of those non-$CO_{ad}$ pathways.

Regarding the mechanism through which cations affect the rate of removal of AOS through the non-$CO_{ad}$ pathways, cations most likely interact with and modify the properties of $OH_{ad}$, as has been proposed previously.[9,15,19,20] However, such an effect should influence all pathways similarly. Therefore, the cation must also modify the reactivity of glycerol itself. This must be facilitated through interactions between glycerol, and possibly reaction intermediates and partial oxidation products, with the cation. While $^1$H-DOSY-NMR discards any cation-induced transport effect, it demonstrates that there is indeed an interaction of the cation with glycerol, stronger with $Li^+$ than with $K^+$, as supported by DFT calculations. As for the nature of this interaction, glycerol must be present in the solvation shell of the cation through non-covalent interactions with its OH groups.

In summary, our results reaffirm the now extended idea that cation-induced trends in electrocatalytic activity are complex and determined by multiple effects unfolding simultaneously. Interactions between the cation and the reactant or reaction intermediates have been claimed as at least partly responsible for cation effects in electrocatalysis for a variety of reactions, including nitrate reduction,[28] hydrogen evolution,[29] CO and $CO_2$ reduction,[30,31] and oxygen evolution,[32-34] which highlights the relevance of our work beyond the oxidation of alcohols and polyols. However, with just a couple of exceptions,[33,34] all those claims were based exclusively on computational calculations. This is the first time, to the best of our knowledge, that such interactions have simultaneously been proven to exist experimentally and shown to necessarily influence an electrocatalytic process.

## Methods

All Teflon and glassware was cleaned by first immersing in a concentrated aqueous solution of $KMnO_4$ + NaOH for 24 hours, followed by rinsing with an acidified aqueous solution of $H_2O_2$:$H_2O$, approx. 9:1 30% m/v $H_2O_2$ (Extra Pure SLR, Fisher) with 2-3 drops of 95% $H_2SO_4$ (Extra Pure SLR, Fisher). This step quickly dissolves any manganese precipitates formed during the cleaning with $KMnO_4$ + NaOH, and is followed by successive boiling and rinsing in ultra-pure water (Elga Veolia, 18.2 MΩ), a minimum of four times. Cells, flasks and so on, are subsequently filled with ultra-pure water until needed.

Electrolyte solutions were prepared in ultra-pure water using high purity $LiOH{\cdot}H_2O$ (99.995% trace metals basis, Fisher), $NaOH{\cdot}H_2O$ (99.996% trace metals basis, Fisher), KOH (99.98% trace metals basis, Fisher) and glycerol (≥ 99.5%, Sigma Aldrich). All experiments were conducted at room temperature and pressure (ca. 1 atm, 20 °C). Electrolytes are saturated with Ar (Zero grade, N50, BOC) under these conditions during each experiment.

UV-Vis Reflectance. The UV-Vis spectroelectrochemical cell was custom-built from Teflon, and houses fused-silica optical windows. The working electrode is a high-purity polycrystalline Pt ($Pt_{poly}$) disc electrode (Alfa Aesar Premion®, 99.997% metals basis) immersed in the electrolyte, hanging vertically from a Pt wire of the same quality. Light reflects from the mirror-polished surface of the disc at 45° of incidence. As such, electrochemical signals come from the whole of the disc (i.e., from its two surfaces plus the rim) and from the small fraction of the suspending wire immersed in the electrolyte, whilst the optical signal comes from the mirror-polished face of the disc reflecting the light beam. A high purity Pt wire is used as a CE, and a home-made reversible hydrogen electrode (RHE) is used as the RE. All potentials in this work are referred to the RHE scale, unless otherwise stated.

The WE and CE are annealed in a propane/air flame for around a minute and air cooled, prior to each experiment. The WE is cycled in the potential window of the experiment until a stable CV is obtained, prior to recording reflectance data, unless stated otherwise. On Pt electrodes, CVs in glycerol-containing electrolytes remain relatively stable over just a few cycles, due to the accumulation of products at the interface. Therefore, when possible, comparing the same cycle number is desirable.

Reflectograms (relative reflectance, $R/R_{max}$, of Pt as a function of potential at constant wavelength, λ) were recorded using a home-made dispersive UV-vis reflectance spectrometer, built from commercially available optics and optomechanics. These include UV-enhanced aluminium coated mirrors (Thorlabs), fused silica lenses (Thorlabs), a monochromator with UV optimised optics (Model 9055, Sciencetech), a 150 W Xe arc lamp (Sciencetech) as the light source and a photomultiplier tube (PMT, Hamamatsu Photonics R955) as the detector. The components are aligned and securely mounted to an anodised-aluminium optical breadboard (Thorlabs). The PMT is powered by a high voltage power supply. The photocurrent generated from the PMT (proportional to the number of photons reflected from the electrode surface per unit time) is passed through a 100 kΩ resistor, the voltage across which is fed into the auxiliary input of a potentiostat (Metrohm Autolab III), via two home-made low pass filters (τ = 50 ms each) arranged in series, and recorded synchronously with the electrochemical measurements. Signal-to-noise (s:n) ratios are between $10^3$ and $3\times10^3$, depending on λ and minor day-to-day variations in optical alignment. The reflectogram is given as $R/R_{max} = V/V_{max}$, where $V$ is the detector output voltage and $V_{max}$ is the maximum detector output voltage obtained across the potential window of the experiment. To further improve the s:n ratio, between 8 and 10 reflectograms were recorded in each experiment and signal averaged, bringing the s:n ratio down to $10^3$. Reflectance experiments are performed in the dark inside a Faraday cage with a matte black interior and covered in a black sheet, to provide electromagnetic shielding and minimise stray light reaching the PMT. A diagram and image of the experimental set-up can be found in section S1 (Figs. S1 and S2) of the supporting information (SI).

ATR-SEIRAS. Time-resolved ATR-SEIRAS experiments were performed using a 3-electrode configuration and a custom-made glass cell. The WE is a nano-structured $Pt_{poly}$ film deposited on a triangular Si ATR prism bevelled at 60°, the CE a high purity Pt wire prepared as detailed above, and the RE a home-made RHE. ATR-SEIRA spectra were recorded using an iS50R FTIR spectrometer, equipped with a custom-built ATR accessory, using non-polarised light. The spectroscopic signal is collected using a liquid $N_2$-cooled MCT detector. The spectral output is differential, given in absorbance units as $A = -\log(\frac{R_{\text{sample}}}{R_{\text{reference}}})$, where $R_{\text{sample}}$ and $R_{\text{reference}}$ are the sample and background single beam spectra, respectively. A diagram of the home-made spectroelectrochemical cell used for these experiments can be found in section S2 of the SI (Fig. S3), along with a description of the Pt film preparation procedure (SI, section S3). All spectra were collected with a spectral resolution of 8 $cm^{-1}$.

For time-resolved experiments, individual sample spectra were first recorded in each glycerol containing solution with respect to a background recorded at 1.3 V in the absence of glycerol, at incrementally more positive potentials leading up to 1.3 V, to ascertain the potential at which the spectroscopic bands for $CO_{ad}$ are indistinguishable from the non-resonant background. A background spectrum was then recorded at this potential (0.6 V) in the presence of glycerol, a negative potential step into the H adsorption region (0.25 V vs RHE) was applied, and a current transient and real-time spectral series with respect to this background were simultaneously recorded. Each spectrum was composed of a single interferogram, resulting in a time resolution of 120 ms. Integrated intensities for the spectroscopic bands corresponding to $CO_{ad}$ were then obtained from the resulting spectral series. To differentiate these data, it is necessary to smooth the raw integrated intensity data. This was done by fitting the data to an order 9 polynomial, which is always presented overlaying the raw data. The value of this derivative of the fitted data at time $t = 0$, obtained by extrapolation, is proportional to the rate of $CO_{ad}$ formation on the $CO_{ad}$-free Pt surface.

For spectral series recorded during a CV, a fresh background at the same potential as in the time-resolved experiments (0.6 V) was used. The potential was then stepped to 0.1 V prior to starting the CV, with each spectrum being composed of 4 interferograms. At a scan rate of 5 mV $s^{-1}$, this results in a resolution of 2.4 mV per spectrum. The improved s:n obtained from accumulating 4 interferograms allowed derivatives of the integrated intensity of bands of interest to be calculated using only mild (5 point) adjacent averaging of the raw data. Smoothed data are always shown overlaying the raw results.

In all experiments, spectral data acquisition was initiated with a trigger signal sent from the potentiostat (Ivium Compactstat), to ensure good synchronisation between electrochemical and spectroscopic data.

$^1$H-DOSY NMR. Samples were prepared using 100 mM aqueous solutions of glycerol (≥ 99.5%, Sigma-Aldrich), either pure or containing increasing concentrations (50, 100, 250, 500, 750, and 1000 mM) of KOH (semiconductor grade pellets, 99.99% trace metal basis, Sigma-Aldrich) or LiOH (anhydrous, 99.9% trace metal basis, Sigma-Aldrich). All solutions were prepared in deuterated water ($D_2O$), with a final volume of 500 µL, and transferred into 5 mm NMR tubes. No internal reference was added. All reagents were commercially available and used as received, without further purification.

All Diffusion-Ordered Nuclear Magnetic Resonance Spectroscopy (DOSY NMR) measurements were carried out on a 9.4 T Bruker Avance III spectrometer operating at 400.18 MHz for $^1$H nuclei, equipped with a BBI probe containing a *z*-gradient coil producing a maximum nominal gradient strength of 53.5 G $cm^{-1}$. Experiments were conducted at 298.15 K using TopSpin 3.6.3 (Bruker BioSpin) software. The diffusion measurements were performed using the $^1$H-Oneshot pulse sequence[35] with 16 diffusion increments, in which the gradient strength varied quadratically from 10 to 80% of the maximum nominal gradient value. For each increment, 16 scans, 16 dummy scans, and 32k data points were acquired. The diffusion time (Δ, d20) and gradient pulse duration (δ, p30)

were individually optimized for each sample to achieve approximately 80% signal attenuation between the first and last increment for the organic compound signals.

All diffusion data were processed using GNAT 1.2.3 software[36] running in MATLAB R2019a. Fourier transformations were applied with 64k points using a Lorentzian window function of 3 Hz, followed by manual and individual phase and baseline corrections. Diffusion coefficients and their associated errors were obtained by fitting a monoexponential decay function derived from the modified Stejskal-Tanner equation to the signal intensities identified via peak-picking analysis. For glycerol, the global diffusion coefficient corresponds to the average value across nine resolved peaks, with the uncertainty representing the propagated error.

Computational Methods. All molecular structures were initially constructed and pre-optimized using the Rowan Scientific web server (https://www.rowansci.com), employing neural network potentials (NNPs) trained on Meta's Open Molecules 2025 (OMol25) dataset, which comprises over 100 million calculations performed at the ωB97M-V/def2-TZVPD level of theory.[37] The neural network used corresponds to a machine-learning interatomic potential (MLIP) based on Meta's equivariant Smooth Energy Network (eSEN) architecture.[38] Specifically, the OMol25 eSEN Conserving Small NNP was employed as implemented in Rowan, together with the ALPB implicit solvation model for water. Subsequently, complexes between glycerol (GLY) and each cation ($K^+$ and $Li^+$) were generated using the automated computational interaction site screening (aISS) workflow[39] with the default docking algorithm implemented in xTB 6.7.0.[40] Docking calculations were performed at the GFN2-xTB[41] level with the ALPB implicit solvation model for water. This protocol employs a genetic algorithm for the initial search using the xTB-IFF intermolecular force field, followed by refinement with GFN-FF and GFN2-xTB geometry optimizations. The lowest-energy complex was selected for further conformer and rotamer sampling using the Conformer–Rotamer Ensemble Sampling Tool (CREST 3.0.2).[42] Sampling was carried out at the GFN2-xTB level with the non-covalent interaction mode enabled, employing the ALPB solvation model for water and an energy window of 62.7 kJ $mol^{-1}$. The iterative metadynamics - using root-mean-square deviation as collective variables - and genetic crossing (iMTD-GC) workflow was employed to efficiently explore the conformational space of each complex. The resulting conformer ensemble was then re-optimized using the OMol25 eSEN Conserving Small NNP with ALPB for water in meticulous mode to obtain improved geometries prior to DFT calculations in a computationally efficient and rapid manner. Finally, the structures were fully optimized at the ωB97X-D4/def2-TZVPD level with the SMD implicit solvation model for water using the ORCA 6.0.0 program.[43] Gibbs free energies, binding Gibbs free energies (interaction energies), and thermodynamic corrections were calculated at the same DFT level of theory.

## References


1. M. Avramov-Ivic, J. M. Leger, B. Beden, F. Hahn and C. Lamy. Adsorption of glycerol on platinum in alkaline medium: effect of the electrode structure. *J. Electroanal. Chem*. **351**, 285-297 (1993). https://doi.org/10.1016/0022-0728(93)80240-I
2. M. Schell, Y. Xu, and Z. Zdraveski. Mechanism for the electrocatalyzed oxidation of glycerol deduced from an analysis of chemical instabilities. *J. Phys. Chem*. **100**, 18962-18969 (1996). https://doi.org/10.1021/jp961195t
3. J. Schnaidt, M. Heinen, D. Denot, Z. Jusys, R. J. Behm. Electrooxidation of glycerol studied by combined in situ IR spectroscopy and online mass spectrometry under continuous flow conditions. *J. Electroanal. Chem*. **661**, 250-264 (2011). https://doi.org/10.1016/j.jelechem.2011.08.011
4. C. Ye, X. Liu and M. T. M. Koper. The role of cations in hydrogen evolution reaction on a platinum electrode in mildly acidic media. *Chem. Commun*. **166**, 107784 (2024). https://doi.org/10.1016/j.elecom.2024.107784

5. M. C. O. Monteiro, A. Goyal, P. Moerland and M. T. M. Koper. Understanding cation trends for hydrogen evolution on platinum and gold electrodes in alkaline media. *ACS. Catal*. **11**, 14328-15335 (2021). https://doi.org/10.1021/acscatal.1c04268

6. V. Briega-Martos, F. J. Sarabia, V. Climent, E. Herrero and J. M. Feliu. Cation effects on interfacial water structure and hydrogen peroxide reduction on Pt(111). *ACS. Meas. Sci. Au*. **1**, 48-55 (2021). https://doi.org/10.1021/acsmeasuresciau.1c00004

7. A. Goyal, S. Louisia, P. Moerland and M. T. M. Koper. Cooperative effect of cations and catalyst structure in tuning alkaline hydrogen evolution on Pt electrodes. *J. Am. Chem. Soc*. **146**, 7305-7312 (2024). https://doi.org/10.1021/jacs.3c11866

8. E. Perez-Gallent, G. Marcandalli, M. C. Figueiredo, F. Calle-Vallejo and M. T. M. Koper. Structure- and potential-dependent cation effects on co reduction at copper single-crystal electrodes. *J. Am. Chem. Soc*. **139**, 16412-16419 (2017). https://doi.org/10.1021/jacs.7b10142

9. C. Stoffelsma, P. Rodriguez, G. Garcia, N. Garcia-Araez, D. Strmcnik, N.M. Marković and M.T.M. Koper. Promotion of the oxidation of carbon monoxide at stepped platinum single-crystal electrodes in alkaline media by lithium and beryllium cations. *J. Am. Chem. Soc*. **132**, 16127–16133 (2010). https://doi.org/10.1021/ja106389k

10. E. Sitta, B. C. Batista and H. Varela. The impact of the alkali cation on the mechanism of the electro-oxidation of ethylene glycol on Pt. *Chem. Commun*. **47**, 3775-3777 (2011). https://doi.org/10.1039/C0CC05353H

11. P. P. Lopes, D. Strmcnik, J. S. Jirkovsky, J. G. Connel, V. Stamenkovic and N. Markovic. Double layer effects in electrocatalysis: The oxygen reduction reaction and ethanol oxidation reaction on Au(111), Pt(111) and Ir(111) in alkaline media containing Na and Li cations. *Catal. Today* **262**, 41-47 (2016). https://doi.org/10.1016/j.cattod.2015.09.010

12. V. Y. Yukuhiro, A. J. Gibson, E. Sitta, A. Cuesta, P. S. Fernández. Effect of cations on the electro-oxidation of alcohols and polyols on Pt: Activity, selectivity, and mechanistic insights. *Curr. Opin. Electrochem*. **52**, 101705 (2025). https://doi.org/10.1016/j.coelec.2025.101705

13. V. Y. Yukuhiro, R.A. Vicente, P. S. Fernández and A. Cuesta, Alkaline-metal cations affect Pt deactivation for the electrooxidation of small organic molecules by affecting the formation of inactive Pt oxide. *J. Am. Chem. Soc*. **146**, 27745–27754 (2024). https://doi.org/10.1021/JACS.4C09590.

14. G. Melle, M.B.C. de Souza, P. V. B. Santiago, P. G. Corradini, L. H. Mascaro, P. S. Fernández and E. Sitta. Glycerol electro-oxidation at Pt in alkaline media: influence of mass transport and cations. *Electrochim. Acta*. **398**, 139318 (2025). https://doi.org/10.1016/j.electacta.2021.139318.

15. D. Strmcnik, K. Kodama, D. Van Der Vliet, J. Greeley, V.R. Stamenkovic and N.M. Marković. The role of non-covalent interactions in electrocatalytic fuel-cell reactions on platinum. *Nat. Chem.* **1**, 466–472 (2009). https://doi.org/10.1038/nchem.330

16. R. Rizo, J. Fernandez-Vidal, L. J. Hardwick, G. A. Attard, F. J. Vidal-Iglesias, V. Climent, E. Herrero and J. M. Feliu. Investigating the presence of adsorbed species on Pt steps at low potentials. *Nat. Commun*. **13**, 2550 (2022). https://doi.org/10.1038/s41467-022-30241-7

17. R. Rizo, L. Chico-Mesa, R. M. Aran-Ais, V. Climent, E. Herrero and J. M. Feliu. Analysis of the OH coverage on low-coordinated pt sites at low potentials. *ACS Electrochem.* **1**, 351-359 (2024). https://doi.org/10.1021/acselectrochem.4c00107

18. A. Cuesta and C. Gutiérrez. Confirmation by differential reflectance spectroscopy of the transition at 270 nm of CO chemisorbed on Pt in an acid medium. *J. Electroanal. Chem*. **383**, 195-197 (1995). https://doi.org/10.1016/0022-0728(94)03760-Z

19. X. Chen, I. T. McCrum, K. A. Schwarz, M. J. Janik, M. T. M. Koper. Co-adsorption of cations as the cause of the apparent pH dependence of hydrogen adsorption on a stepped platinum single-crystal electrode. *Angew. Chem*. **52**, 15025-15029 (2017). https://doi.org/10.1002/anie.201709455

20. L. Shen, A. Goyal, X. Chen and M. T. M. Koper. Cation effects on hydrogen oxidation reaction on Pt single-crystal electrodes in alkaline media. *J. Phys. Chem. Lett.* **15**, 2911–2915 (2024). https://doi.org/10.1021/acs.jpclett.4c00292

21. P. V. B. Santiago, R. A. G. Oliveira, J. M. Roquetto, N. Akiba, I. Gaubeur, C. A. Angelucci, J. Souza-Garcia and J. M. Feliu. Oxide formation as probe to investigate the competition between water and alcohol molecules for OH species adsorbed on platinum. *Electrochim. Acta*. **317**, 694–700 (2019). https://doi.org/10.1016/j.electacta.2019.06.037

22. L. Pérez-Martínez, L. Balke and A. Cuesta. Reactive and inhibiting species in the electrocatalytic oxidation of glycerol on gold. A study combining in-situ visible reflectance and ATR-SEIRAS. *J. Cat*. **394**, 1-7 (2019). https://doi.org/10.1016/j.jcat.2020.12.010

23. A. J. Gibson and A. Cuesta. Dual-pathway mechanism and nonlinear dynamics in the electrooxidation of methanol on platinum. *ACS. Catal.* **15**, 12598-12609 (2025). https://doi.org/10.1021/acscatal.5c02987

24. D. S. Mekazni, R. M. Aran-Ais, A. Ferre-Vilaplana and E. Herrero. Why methanol electro-oxidation on platinum in water takes place only in the presence of adsorbed OH. *ACS Catal.* **12**, 1965–1970 (2022). https://doi.org/10.1021/acscatal.1c05122

25. W. M. Haynes. Fluid properties: viscosity and density of aqueous hydroxide solutions. *CRC Handbook of Chemistry and Physics, 97th ed.*, section 6, p. 248 (CRC Press. 2016).

26. G. Hussain, L. Perez-Martinez, J. Le, M. Papasizza, G. Cabello, J. Cheng and A. Cuesta. How cations determine the interfacial potential profile: Relevance for the $CO_2$ reduction reaction. *Electrochim. Acta* **327**, 135055 (2019). https://doi.org/10.1016/j.electacta.2019.135055

27. A. Cuesta, A. Couto, A. Rincon, M.C. Perez, A. Lopez-Cudero and C. Gutierrez. Potential dependence of the saturation CO coverage of Pt electrodes: The origin of the pre-peak in CO-stripping voltammograms. Part 3: Pt(poly). *J. Electroanal. Chem*. **586**, 184‑195 (2006). https://doi.org/10.1016/j.jelechem.2005.10.006

28. R.-Y. Zhou, S. Zheng, R. Ma, Y.-H. Wang, M. Zhao, C. Zhai, J.-C. Dong, F. Pan, J.-F. Li. Deciphering cation stabilized $*NO_2$ at the molecular level in electrocatalytic nitrate reduction. *J. Am. Chem. Soc.* **148**, 425-433 (2026). https://doi.org/10.1021/jacs.5c13376

29. J. T. Bender, A. S. Petersen, F. C. Ostergaard, M. A. Wood, S. M .J. Hefferman, D. J. Milliron, J. Rossmeisl, J. Resasco. Understanding cation effects on the hydrogen evolution reaction. *ACS Energy Lett.* **8**, 657-665 (2023). https://doi.org/10.1021/acsenergylett.2c02500

30. Y. Xu, Z. Xia, W. Gao, H. Xiao, B. Xu. Cation effect on the elementary steps of the electrochemical CO reduction on Cu. *Nat. Catal.* **7**, 1120-1129 (2024). https://doi.org/10.1038/s41929-024-01227-z

31. M. C. O. Monteiro, F. Dattila, B. Hagedoorn, R. García-Muelas, N. López, M. T. M. Koper. Absence of $CO_2$ electroreduction on copper, gold and silver electrodes without metal cations in solution. *Nat. Catal.* **4**, 654–662 (2021). https://doi.org/10.1038/s41929-021-00655-5

32. J. Zaffran, M. B. Stevens, C. D. M. Trang, M. Nagli, M. Shehadeh, S. W. Boettcher, M. C. Toroker. Influence of electrolyte cations on Ni(Fe)OOH catalyzed oxygen evolution reaction. *Chem. Mater.* **29**, 4761-4767 (2017). https://doi.org/10.1021/acs.chemmater.7b00517

33. H. Komiya, K. Obata, O. Sekizawa, K. Nitta, K. Xu. M. Wada, K. Takanabe. Mass activity elucidation of cobalt-based oxygen evolution catalysis utilizing depth-resolved spectroscopy in

the presence of various cations with chloride. *Angew. Chem. Int. Ed.* **64**, e202501579 (2025). https://doi.org/10.1002/anie.202501579

34. A. C. Garcia, T. Touzalin, C. Nieuwland, N. Perini, M. T. M. Koper. Enhancement of oxygen evolution activity of nickel oxyhydroxide by electrolyte alkali cations. *Angew. Chem. Int. Ed.* **58**, 12999-13003 (2019). https://doi.org/10.1002/anie.201905501
35. M. D. Pelta, G. A. Morris, M. J. Stchedroff, S. J. Hammond. A one-shot sequence for high-resolution diffusion-ordered spectroscopy. *Magn. Reason. Chem*. **40**, 147–152 (2002). https://doi.org/10.1002/mrc.1107
36. L. Castanar, G. Dal Poggeto, A. A. Colbourne, G. A. Morris and M. Nilsson. The GNAT: A new tool for processing NMR data. *Magn. Reson. Chem*. **56**, 546-558 (2018). https://doi.org/10.1002/mrc.4717
37. D. S. Levine, M. Shuaibi, E. W. C. Spotte-Smith, M. G. Taylor, M. R. Hasyim, K. Michel, I. Batatia, G. Csányi, M. Dzamba, P. Eastman, N. C. Frey, X. Fu, V. Gharakhanyan, A. S. Krishnapriyan, J. A. Rackers, S. Raja, A. Rizvi, A. S. Rosen, Z. Ulissi, S. Vargas, C. L. Zitnick, S. M. Blau, B. M. Wood. The Open Molecules 2025 (OMol25) Dataset, Evaluations, and Models. Preprint at https://doi.org/10.48550/arXiv.2505.08762 (2025).
38. X. Fu, B. M. Wood, L. Barroso-Luque, D. S. Levine, M. Gao, M. Dzamba, C. L. Zitnick. Learning smooth and expressive interatomic potentials for physical property prediction. Preprint at https://doi.org/10.48550/arXiv.2502.12147 (2025).
39. C. Plett and S. Grimme. Automated and Efficient Generation of General Molecular Aggregate Structures**.** *Angew. Chem. Int. Ed*. **62**, e202214477 (2023). https://doi.org/10.1002/anie.202214477
40. C. Bannwarth, E. Caldeweyher, S. Ehlert, A. Hansen, P. Pracht, J. Seibert, S. Spicher, S. Grimme. Extended tight-binding quantum chemistry methods. *WIREs Comput. Mol. Sci.* **11**, e1493 (2021). https://doi.org/10.1002/wcms.1493
41. C. Bannwarth, S. Ehlert and S. Grimme. GFN2-xTB - An accurate and broadly parametrized self-consistent tight-binding quantum chemical method with multipole electrostatics and density-dependent dispersion contributions. *J. Chem. Theory Comput.* **15**, 1652–1671 (2019). https://doi.org/10.1021/acs.jctc.8b01176
42. P. Pracht, S. Grimme, C. Bannwarth, F. Bohle, S. Ehlert, G. Feldmann, J. Gorges, M. Müller, T. Neudecker, C. Plett, S. Spicher, P. Steinbach, P. A. Wesołowski, F. Zeller. CREST - A program for the exploration of low-energy molecular chemical space**.** *J. Chem. Phys.* **160**, 114110 (2024). https://doi.org/10.1063/5.0197592
43. F. Neese, F. Wennmohs, U. Becker, C. Riplinger. The ORCA quantum chemistry program package. *J. Chem. Phys*. **152**, 224108 (2020). https://doi.org/10.1063/5.0004608

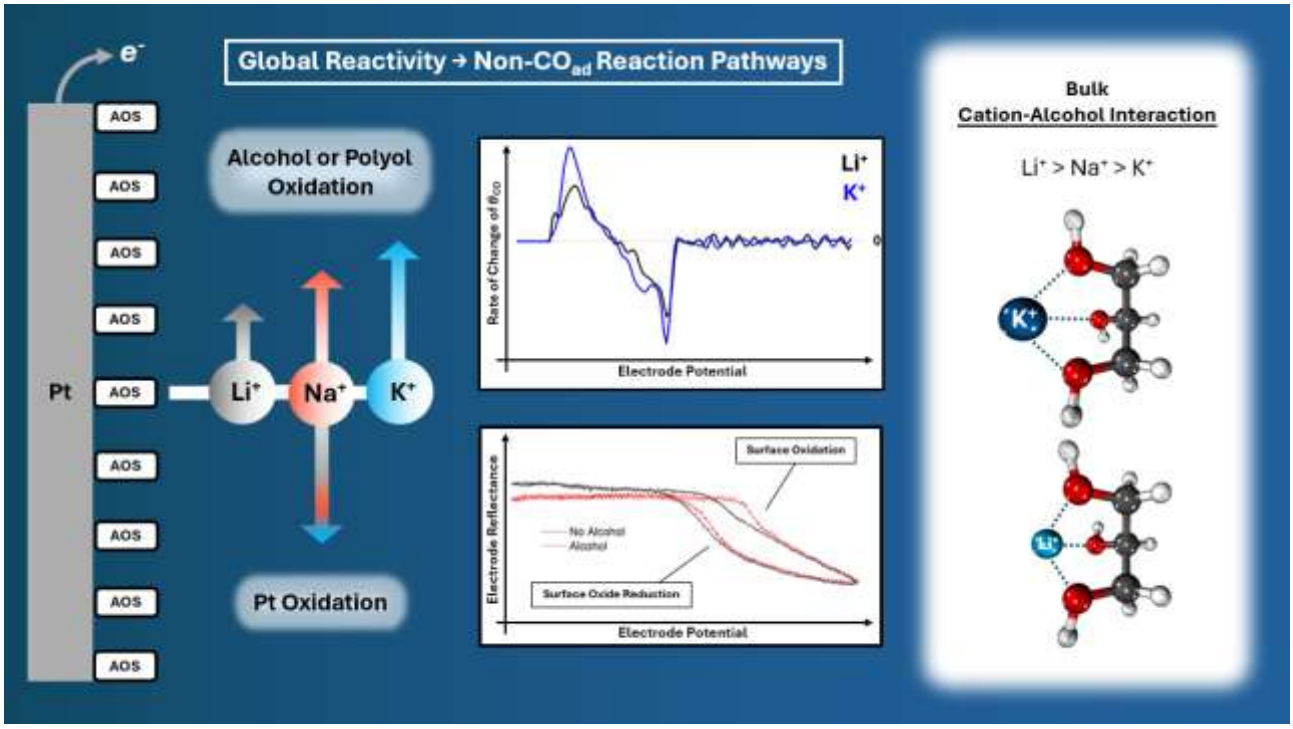
## Acknowledgments

The support of a PhD scholarship from The Carnegie Trust for the Universities of Scotland (PHD012002) is gratefully acknowledged. T.L.G.C. and C.F.T. gratefully acknowledge financial support from the São Paulo Research Foundation (FAPESP, Grant Nos. #2020/10246-0, #2021/05081-5, #2022/11152-5 and #2023/07116-6) and the LIRMN facility (RRID:SCR_027247) from CEMUIQ–UNICAMP. V.Y.Y. acknowledges the support of Conselho Nacional de Desenvolvimento Tecnológico (CNPq) [Grant number: 141281/2023-5]. This study was financed in part by the Coordenação de Aperfeiçoamento de Pessoal de Nível Superior – Brasil (CAPES) – Finance code 001.

## Conflicts of Interest

No conflicts of interest to declare.

## Graphical Abstract



## Supplementary Files

This is a list of supplementary files associated with this preprint. Click to download.

- SIAJGTLGCVYYCFTPSFACCationeffectsGOR.docx